

POROSITY FORMATION IN AL-SI- CU ALLOYS

A.M. SAMUEL¹, S.A. ALKAHTANI², H.W. DOTY³&F.H. SAMUEL^{1,4}

^{1,4}*Département des Sciences appliquées, Université du Québec,*

Chicoutimi (Québec), Canada

²*Industrial Engineering Program, Department of Mechanical Engineering, College of Engineering, Sattam*

Bin Abdulaziz University, Al Kharj, Saudi Arabia

³*General Motors, Materials Engineering, Pontiac, USA*

ABSTRACT

The present study was performed on an Al-Si-Cu 319-type alloy using an end-chill mold, while varying the cooling rate along the solidification axis. Good fits for response parameters of percent porosity, maximum pore area, average pore area, maximum pore length and average pore length were obtained from the statistical analysis of the porosity data for the end-chill mold samples. These results strongly support the porosity formation observed in an aluminum 319.2 alloy reported in an earlier study. Tensile samples were T6 heat-treated, and the data obtained from these samples were analyzed statistically.

KEYWORDS:Al-Si-Cu 319-Type Alloy, Maximum Pore Area, End-Chill Mold Samples

Received: Nov 25, 2015; **Accepted:** Dec 19, 2015; **Published:** Jan 05, 2016; **Paper Id.:**IJMMSEFEB20161

INTRODUCTION

Two important factors that determine the eventual quality and properties of aluminium cast components are the solidification rate and porosity. Solidification rate affects the microstructure, as well as the porosity formed, while porosity affects the surface quality, soundness, corrosion resistance and other properties. Apart from solidification rate, microstructural control is also achieved through grain refinement and modification, where small additions of Al-Ti-B and Al-Sr master alloys, respectively, provide the means for producing refined microstructures and the required morphology of constituent phases [1-7].

With regards to porosity, its formation is attributed mainly to two effects: (i) shrinkage, resulting from the volume decrease accompanying solidification, and (ii) the evolution of dissolved gases, resulting from the decrease in solubility of these gases in the solid, as compared to the liquid metal. Hydrogen, the only gas capable of dissolving to a significant extent in molten aluminum but exhibiting very low solubility in the solid state, is mainly responsible for the gas porosity in the casting, together with the pressure during solidification, the chemical composition and solidification range of the alloy, and the solidification rate. Shrinkage porosity can also occur as "microshrinkage" or "microporosity", dispersed in the interstices of dendritic solidification regions. Limited or inadequate liquid metal feeding in the dendritic solidification area gives rise to this type of porosity [8-10].

Grain refining, modification and the inclusion content of the melt also influence porosity formation. Melt cleanliness, with particular regard to the presence of oxides and inclusions, is recognized as an important factor that influences hydrogen gas nucleation [11]. More often than not, the various factors contributing to porosity manifest themselves simultaneously, interacting with each other to develop the resulting porosity observed.

Although porosity in aluminum alloys has been investigated, detailed systematic data on different alloy systems in terms of parametric studies of the porosity formation and distribution is generally not

available. In the case of the cast aluminum alloy 319, which ranks as one of the commercially important alloys used in automotive applications on account of its excellent casting characteristics and good mechanical properties, for instance, relatively little is to be found in the literature on such studies, as compared to the A356 automotive alloy [12, 13]. In fact, studies reported by our group [14, 16] appear to be among the few that cover porosity formation in Al-Si-Cu-Mg alloys, compared to numerous investigations carried out on Al-Si cast alloys.

This lack of design data, particularly in the know-how of controlling the formation of porosity and its effect on secondary properties (e.g., fatigue, wear, corrosion, etc.) in these alloys poses constraints on their applicability. Addressing this issue by providing such data would certainly remedy the situation. The aim of the present project, therefore, was to distinguish the different factors affecting porosity and to determine their individual and combined effects on porosity formation in 319 alloy, in relation to the product quality, the systematic data generated from the work to be used to obtain a response surface model of the porosity behaviour of this alloy.

The present work was under taken to:

- Study of the effect of hydrogen content (0.1-0.4 ml/100 g Al), modification (Sr: 0-300 ppm) and grain refinement (TiB₂: 0-0.02 wt. %) on the porosity formation and distribution in 319 commercial aluminum alloy.
- Parametric study of the evolution of porosity in the Al-Si-Cu-Mg system in order to develop a response surface model of the porosity behaviour of this alloy system as a function of alloy and process parameters.
- Correlating of porosity with tensile properties: yield strength (YS), ultimate tensile strength (UTS) and ductility or fracture elongation (El.%).

Experimental Procedure

The 319.2 aluminum alloy used in this study was supplied in the form of 12.5-kg ingots. The chemical composition of the as-received alloy is shown below in Table 1. The ingots were melted in a silicon carbide crucible of 7-kg capacity, using an electric resistance furnace. The melting temperature was held at 735±5°C. At this temperature, the molten metal was either degassed using high purity argon (melt hydrogen content ~0.1 ml/100 g Al - designated H1), or gassed (melt hydrogen content 0.2-0.24 ml/100 g Al - designated H2 or ~0.32-0.36 ml/100g Al - designated H3). Melts were also modified with strontium (with Sr levels of ~70-90 ppm - designated S1, 120-180 ppm - designated S2, 250-310 ppm - designated S3) using Al-10 wt. % Sr master alloy, and grain-refined by means of Al-5 wt. % Ti-1 wt. % B master alloy to obtain a 0.02 wt. % Ti content (designated T). The melt hydrogen level was monitored using an AlScan™ unit and was also determined from "Ransley" samples obtained from Ransley mold castings of each melt, using the Leco vacuum fusion technique [17]. For each pouring, samplings for chemical analysis were also taken. The samples were analyzed using inductive plasma couple (ICP) or spectrometric analysis elsewhere.

Casting was carried out using a rectangular-shaped end chill mold made of refractory material (to ensure directional solidification and good thermal insulation), where the molten metal was poured through 8 pores/cm (i.e. 20 ppi) ceramic foam filter discs fitted into the riser (above the sprue) to avoid incident inclusions. Figure 1 shows a schematic diagram of the end chill mold, the chill consisting of a copper box at the bottom through which cold water was circulated. Prior to

casting, the mold was preheated to 150°C to drive out moisture. The water was turned on the moment the liquid metal had half-filled the mold. To reduce heat loss from the open surface, the top of the end chill mold was covered with an insulated ceramic board as soon as the mold was completely filled.

Such a casting arrangement produced ingots with solidification rates which decreased with increasing distance from the chill. Obtained ingot dimensions were approximately 7 cm x 14 cm x 20 cm. Table 2 indicates the average dendrite arm spacings (DAS) and local cooling rates that were obtained (from the respective microstructures and thermal analysis cooling curves), corresponding to different distances from the chill end.

The number of castings representing all the conditions studied was 24 in all, covering the H, HS, HT and HTS series, with H and S further divided as H1, H2 and H3, and S1, S2 and S3 according as the 3 levels of hydrogen or strontium selected for a particular casting (H, S and T denoting the hydrogen, strontium and grain refiner levels of the melt from which the casting was obtained). Table 3 enumerates the different castings that were produced. For each condition, three identical castings were made, one for microstructural analysis and porosity measurements, two for tensile property measurements. Samples were sectioned from the cast blocks in the horizontal orientation at varying heights (5, 10, 20, 40 and 100 mm) above the water-chilled copper base, from which metallographic or tensile test sheet specimens were prepared for metallographic observations or tensile testing purposes, respectively. Table 4 lists the actual chemical compositions.

Five samples (2 cm x 3 cm) from each end-chill casting were obtained, cut from the central portion of the casting at the five levels of 5, 10, 20, 40 and 100 mm above the end-chill bottom, as mentioned previously. Microstructural changes on polished surfaces of these metallographic samples were examined using optical microscopy. The α -aluminum DAS, eutectic Si, and β -iron Al₅FeSi phase particle characteristics and the porosity were analysed/quantified using a Clemex image analyser in conjunction with the optical microscope (Olympus PMG3).

Corresponding to the 24 end-chill castings listed in Table 3, a total of 120 metallographic samples (24 castings x 5 levels) was obtained for which porosity measurements were carried out using image analysis (Clemex image analyser in conjunction with an Olympus PMG3 optical microscope). For these measurements, the number of fields ("field" representing the field of view of the optical microscope and covering an area of $2.23 \times 10^6 \text{ sq}\mu\text{m}$ at 50X magnification) examined were chosen so as to cover the entire area of the specimen. That is to say, the entire surface of the specimen is traversed in a regular, systematic fashion and the porosity (or other particle/phase) characteristics noted for the selected number of fields. In the present case, one hundred fields were required at 50X magnification to cover the entire sample surface area. The parameters measured were the area percent porosity (i.e., porosity % measured over a constant sample surface area), pore area, pore length and pore aspect ratio, as well as the pore count.

Sheet samples for tensile testing (60 mm x 20 mm x 3 mm) were obtained from each end-chill casting at the same five levels of 5, 10, 20, 40 and 100 mm above the chill end, the samples being cut in such a way that their centerlines passed through the five levels. The samples were heat treated at 180°C/8 hours, air cooled, and tensile tested at room

temperature using an MTS Servo-hydraulic machine at a strain rate of 4×10^4 /s. Tensile properties, viz., yield strength at 0.2% offset strain, ultimate tensile strength, and fracture elongation were derived from the data acquisition system attached to the testing machine.

Samples for SEM examination were sectioned from the tensile-tested specimens about 1 cm below the fracture surface, and were then mounted with care for fracture surface examination. The fracture surface for each of the tested specimens was examined using a JEOL 840A scanning electron microscope operating at 15KV and 3A.

RESULTS AND DISCUSSIONS

Earlier studies [18-20] have shown that β -platelets are very active as pore nucleation sites, in that small pores are often found nucleated along the long sides of the platelets. Such a mechanism is expected to result in an increase in pore density, which is strongly related to the metal feedability or the ease with which the molten metal can flow into the different sections of the casting mold. However, in spite of the harmful effect of the β -platelets as pore nucleation sites, their presence seems to limit pore growth. Figure 2 shows how the β -platelets limit the lateral growth of both gas and shrinkage pores. Proper control of this phase thus becomes important from both properties and porosity points of view. Essential features observed with respect to the occurrence of the β -Al₅FeSi phase in the current study are as follows:

- The DAS critically affects the size of the β -platelets, the latter being indicative of the volume fraction of the phase obtained in the sample. Figure 3 compares the microstructures of H1 alloy samples (degassed alloy, no melt treatment) obtained at 5 mm and 100 mm levels above the chill end showing how they are extremely difficult to discern at the highest cooling rate, but are observed in relative abundance at the slow cooling rate of the 100 mm (above the chill end) sample.
- In the unmodified alloy (H1), sympathetic (preferential) nucleation of the platelets is observed, leading to the branching of several platelets from a parent needle. Addition of Sr is seen to reduce this effect, the Sr poisoning the nucleation sites and assisting in the dissolution of the β -platelets. An addition of 300 ppm Sr (H1S3 alloy) is seen to accelerate the dissolution process, leading to the fragmentation of the platelets into smaller segments (cf. 60- 80 μ m with 120-1200 μ m in the untreated H1 alloy).
- A tendency for thickening of the β -platelets is observed with grain refining, along with the sympathetic nucleation/branching effect noted in the untreated alloy. The thickening takes place via a step-like motion of ledges as shown in Figure 4. Brittle fracture of thick platelets was observed to occur different from the fragmentation that occurs due to Sr-modification.
- A comparison of the β -platelets densities for H1, H1T, H1S3 and H1TS3 alloys at the 100mm level (DAS ~90 μ m) reveals that the H1S3 alloy sample gives the lowest platelet density (Figure 5). Use of a grain refiner decreases the beneficial effect obtained with Sr addition.

The microstructure of H1 alloy at 5 mm distance from the chill showed very small and well scattered pores, At 100 mm distance from the chill, pores were seen in the interdendritic regions, disconnected, their lengths approximately the same as the dendrite arms or even less, Figure 6(a).

The microstructure of H1S3 alloy at 5 mm distance from the chill did not reveal much change in porosity size and distribution above what was observed in the corresponding H1 sample. However, the structure changed dramatically as the

distance from the chill increased to 100 mm (Figure 6(b)). The pores were rounded, and an increase in pore size and percentage porosity was observed.

In the grain-refined alloy (H1T), a well dispersed distribution of small pores was observed, with the pores occurring either at the grain boundaries or within the grains. The variation in percentage porosity with DAS for degassed and filtered melt castings of the H1 alloys under different melt treatment conditions is summarized in Figure 7. It is well established that hydrogen is the strongest determinant of all the parameters that contribute to porosity formation. This was clearly evidenced from the microstructures of the H3 alloy samples. At a 5-mm distance from the chill, two distinct pore morphologies, elongated and rounded, could be observed, Figure 8(a). At a 100-mm distance, however, the majority of pores were rounded, Figure 8(b). The hydrogen-strontium interaction effect on porosity (H3S3 alloy) resulted in pores that were mostly round as opposed to the mixture of rounded and elongated forms observed in the case of H3 alloy (at a 5-mm distance from the chill). This treatment was also associated with an increase in the area pore density. An increase in the cooling rate (i.e., at 100 mm above the chill) resulted in pores that were larger and more spherical than those observed in H3 alloy.

Samples obtained from the H3TS3 alloy and etched in Keller's reagent were examined to determine the nucleation mechanism of pores. At low cooling rates (5 mm distance from the chill) the pores (elongated or rounded) were mostly found nucleated at or along the grain boundaries. At intermediate cooling rates (20 mm distance from the chill), while most of the pores were nucleated in the intergranular regions, some were observed in the interdendritic regions, Figure 9 (thick white arrow shows the presence of TiB_2 at the interiors of the pores). At the highest cooling rate (100 mm distance from the chill) also, the possibility of pore nucleation in the intergranular regions was still evident.

Porosity formation and growth in aluminum alloy castings has been extensively investigated, both experimentally and theoretically, using mathematical modelling (refer to the works listed in the two overviews in ref. [7]). In order to link the two, statistical analysis using data reduction techniques is one of the more recent means increasingly being applied to quantitatively predict porosity formation in such alloy castings, based on the results obtained from a planned set of experiments (variously termed factorial or fractional factorial designs [14, 15] according to the designed input), where the response parameters (those of porosity) can be quantitatively related to the predictor or controlling parameters determined by the alloying and melt conditions set by the experiments.

Such statistically designed experiments are very efficient in that they provide a fixed amount of information with much less effort than the classic approach using one variable at a time would demand. More importantly, they provide information about the interactions between the controlling variables, which constitutes a very significant factor in the search for optimum conditions, in this case, that of obtaining quality castings containing minimum porosity. The effectiveness of this approach - termed Response Surface Methodology - has been variously demonstrated in the case of an A356 alloy by Tynelius *et al.* [7] and in Al-Si-Cu-X alloys by Roy [17] and Roy *et al.* [22].

Apart from presenting the results in a simple manner and extracting the maximum information possible from a given set of experiments, statistical methods can also aid the experimenter to arrive at the correct conclusions in spite of variability in the experimental results [15]. Among the different analytical methods available, that of multiple regression analysis, using stepwise reduction, was selected, for the above-mentioned reasons, namely, the ability of this technique to detect and evaluate the interactive effects of the several predictor parameters on the response parameters.

As previously mentioned, the porosity data obtained for the 135 end-chill samples was further analysed to obtain (i) pore density vs. pore area and (ii) pore density vs. pore length distributions, from which the average and maximum pore area/pore length values and respective pore densities were determined for the two parts of the distribution curves representing small and large pores. The area percent porosity was also determined in each case. These values constitute the *response* parameters that are obtained as a result of the alloy parameters (chemical composition) and thermal parameters (cooling rate and solidus velocity) of each sample (viz., the predictor or controlling parameters). The final data set comprising all of these parameters was analyzed using multiple regression analysis, to derive contour plots to predict the effect (independent and/or interactive) of the various predictor parameters on the porosity.

It is not within the scope of the present work to go into the details of the procedures and various tests conducted in such an analysis; these are well covered in standard text books such as those of Box, Hunter and Hunter [23], Davies [24] and Casella [25]. Essentially, for any statistical analysis, the four essentials required are: (i) the experimental data collection (results) or population, (ii) the mean value of these results, (iii) a quantitative means of representing the results, e.g., by the standard deviation or variance and (iv) the means to assess the validity of the results/conclusions, using a test of significance. Such a test gives the probability that the difference between a sample value and a hypothesized value is due only to sampling error. For a sample value to be statistically significant, this difference must be low. The mean and standard deviation (or variance) enables us to indicate the precision with which we can state the characteristics of the population or data collection by quoting confidence intervals or limits within which the true value very probably lies [23].

The multiple regression analysis of the porosity data obtained in the present study was carried out using StateSoftStatistica is a comprehensive, integrated statistical data analysis, graphic and data base management system featuring a wide selection of basic and advanced analytical procedures including a Multiple Regression module. The latter program, covering a vast range of regression techniques including simple, multiple, stepwise, nonlinear (polynomial, exponential, log, etc.) and Ridge regression, is capable of calculating a comprehensive set of statistics including the complete regression table.

A forecasting routine allows the user to perform "what-if" analyses and to interactively compute predicted scores based on user-defined values of predictors. Extremely large regression designs (up to 300 variables) can be analysed. Multiple response variables can be processed in pairs, and various options are available for counting missing data. The independent variables (or controlling parameters) comprised the alloy parameters, *viz.*, Si, Cu, Zn, Fe, Mg, Mn, Ti compositions, as well as the Sr and hydrogen (H) levels analysed in each case, the grain refiner (GR) addition (taken as 0 or 0.02%), the DAS (μm), and the cooling time (TS-obtained from cooling curves) and solidus velocity (VS), giving a total of 13 variables.

Predictor terms (including interaction parameters) were constructed using these variables and tested for their ability to predict the response parameters (or dependent variables) of percentage porosity, average and maximum pore lengths/pore areas, and the respective pore densities for both the exponential and irregular parts of the pore distribution curves in each case. Following these steps, data sets of 135 cases with 55 variables were obtained for the end-chill.

The two data sets were then explored using the StateSoftStatistica software program, until those predictor terms that gave the best possible fit to the data set were found. This was done by evaluating the R^2 value (that indicated the fraction of variance in the data set, an R^2 value of one representing a perfect correlation), the *t*-value (which assessed the relative strength of each predictor term), and the *p*-level or significance number (which measured the relative significance

of each term), the closer to zero the p-level, the more certain the relationship between the predictor term and the response parameter.

In the case of the end-chilled samples, good fits were obtained for almost all the response parameters, viz., for percentage porosity, and maximum pore area, average pore area, maximum pore length, and average pore length for the irregular part of the porosity distribution curves (*i.e.*, big pores), with R^2 values ranging between 0.873 and 0.768. The maximum pore area showed the highest R^2 value (0.873), with percentage porosity (0.832) and average pore area (0.831) following closely. For all models, the predictor variables were H, DAS, Sr, Ti and Mg, with cooling time (TS) and Cu as additional predictors in some of the models, like those for percentage porosity and average pore area.

Table 5 summarizes the predictor variables used to develop the various response surface models (response parameters), and the t-values and significance levels obtained for each predictor in the respective cases. As can be seen, hydrogen is the parameter that has the greatest impact on the percentage porosity, followed by the DAS, and then Sr, these parameters showing the highest t-values and zero significance levels (the 0.00000 p-levels quoted in the table are actually 0.000000). However, as far as the other response parameters are concerned, *i.e.*, those that correspond to the pore size (pore area/pore length), it is the DAS that has the greater influence compared to hydrogen. The strongest impact of DAS is on the maximum pore area, with a t-value of 22.35 compared to 8.721 for hydrogen.

Comparing the effects of strontium and titanium (*i.e.*, grain refiner) additions, strontium has the greater influence on the percentage porosity and pore areas (average and maximum). The pore lengths (average and maximum), however, are controlled more by titanium than by strontium. This is to be expected, in view of the effect that grain refiner addition has on reducing the grain size and, hence, the grain boundary facets along which the pores form, in other words, the pore lengths.

The above results strongly support our microstructural observations and qualitative analysis of porosity distribution reported earlier on in our work (see publications 1 and 2 quoted at the end of this report). Yet another interesting observations made from Table 5 is that Mg appears to have an influence comparable to that of hydrogen on the pore size response parameters of area and length. However, its overall effect on the percentage porosity is much less compared to that of hydrogen, DAS and strontium.

Figures 10(a) through (c) show the 3D surface plots obtained from directional solidification mold under different working conditions. For a given hydrogen level, decreasing the cooling rate (Figure 10(a)) leads to remarkable increase in percentage of porosity. Addition of Sr up to 350 ppm also contributes to porosity formation but to a lesser extent compared to that obtained from cooling rate (Figure 10(b)). Grain refining using TiB_2 is the only parameter that would reduce the percentage of porosity (Figure 10(c)).

CONCLUSIONS

Based on an analysis of the results obtained from the present study, the following points may be summarized.

- With respect to cooling rate (obtained as a function of DAS) as one parameter, the interaction effect of other parameters, namely hydrogen (H_2), modifier (Sr) and grain refiner (TiB_2) levels on the porosity follows the order: $H_2 > Sr > TiB_2$.
- At high cooling rates, pore nucleation takes place predominantly in intergranular regions. The pore morphology is mostly elongated, the pores being observed to lie along the grain boundaries (due to the long freezing range of the

alloy). The probability of pore nucleation taking place in interdendritic regions increases at higher cooling rates, and the pore morphology tends to be more rounded, as well.

- Although strontium addition increases the porosity, the beneficial effect of Sr modification (i.e., with respect to modification of the eutectic silicon particles), however, improves the alloy ductility. Sr is also seen to poison the nucleation sites of the β -Al₅FeSi phase platelets observed in the alloy structure (these platelets act as active pore nucleation sites and are also detrimental to the alloy tensile properties).
- Fragmentation and dissolution of the β -platelets takes place with increasing Sr levels, and the harmful effect of the iron intermetallic is greatly reduced. Comparisons of untreated, modified and grain-refined alloys show that the modified alloy contains the lowest amount of the iron phase.
- Good fits for response parameters of percentage porosity, maximum pore area, average pore area, maximum pore length, and average pore length are obtained from the statistical analysis of the porosity data for the end-chill mold samples. The results strongly support the microstructural observations/qualitative analysis of porosity formation in 319.2 alloy.
- Hydrogen has the greatest influence on percentage porosity, followed by DAS and Sr, for the end-chill samples. However, pore size is controlled more strongly by the DAS than by hydrogen, the strongest impact of DAS being on the maximum pore area.
- While percentage porosity and pore area are more influenced by strontium than by titanium (grain refiner) addition, pore length is controlled to a greater extent by the latter.
- For the end-chill case, magnesium is also observed to have an influence comparable to that of hydrogen on the pore size (area/length).

ACKNOWLEDGEMENTS

The authors would like to thank Ms. Amal Samuel for enhancing the image work in the present study.

REFERENCES

1. R.J. Garino and S. Wakesberg, "Automobile material choices", *Scrap Processing and Recycling*, **51**(1994), pp. 101-105.
2. Z. Ma, "Effect of Fe-Intermetallics and Porosity on Tensile and Impact Properties of Al-Si-Cu and Al-Si-Mg Cast Alloys", *Ph.D. Thesis, Université du Québec à Chicoutimi, Canada*, Nov., 2003.
3. A.M. Samuel, F.H. Samuel and H.W. Doty, "Observations on the Formation of β -Al₅FeSi Phase in 319 type Al-Si Alloys," *Journal of Materials Science*, **31**(1996), pp. 5529-5539.
4. J. Espinoza-Cuadra, P. Gallegos-Acevedo, H. Mancha-Molinar and A. Picado, "Effect of Sr and Solidification Conditions on Characteristics of Intermetallic in Al-Si 319 Industrial Alloys," *Materials and Design*, **31**(2010), pp. 343-356.
5. L. Liu, A.M. Samuel, F.H. Samuel, H.W. Doty and S. Valtierra, "Role of iron in relation to silicon modification in Sr-treated 319 and 356 alloys," *International Journal of Cast Metals Research*, **16**(2003), pp. 397-408.
6. L. Liu, A.M. Samuel, F.H. Samuel, H.W. Doty and S. Valtierra, "Characteristics of alpha-dendritic and eutectic structures in Sr-treated Al-Si casting alloys," *Journal of Materials Science*, **39**(2004), pp. 215-224.

7. K. Tylenius, J.F. Major and D. Apelian, "Optimization of Castings parameters for Production of Sound Al Castings: A Response Surface Methodology Approach," *AFS Transactions*, **101**(1993), pp. 401-413.
8. H. R. Ammar, A. M. Samuel and F.H. Samuel, "Effects of surface porosity on the fatigue strength of AE425 and PM390 hypereutectic Al-Si casting alloys at medium and elevated temperatures," *Materials Science and Engineering A*, **473**(2008), pp.58-64.
9. G.A. Edwards, G.K. Sigworth, C.H. Cáceres, D.H. St. John and J. Barresi, "Microporosity Formation in Al-Si-Cu-Mg Casting Alloys," *Paper to be presented at the 1997 AFS Casting Congress in Seattle*, 25 pp.
10. A.M. Samuel and F.H. Samuel, "A metallographic study of porosity and fracture behavior in relation to the tensile properties in 319.2 end chill castings," *Metallurgical and Materials Transactions A*, **26**(1995), pp. 2359-2372.
11. N. Roy, A.M. Samuel and F.H. Samuel, "Porosity formation in Al-9 Wtpt Si-3 Wtpt Cu alloy systems: Metallographic observations," *Metallurgical and Materials Transactions A*, **27A**(1996), pp. 415-429.
12. C. Dupuis, Z. Wang, J-P. Martin and C. Allard, *Light Metals 1992*, E.R. Cutshall (ed.), *The Minerals, Metals and Materials Society*, 1992, pp. 1055-1068.
13. D. L. McLellan, "Tensile Properties of A357-T6 Aluminum Castings," *Journal of Testing & Evaluation*, Vol. 8, No. 4, July 1980, pp. 170-176.
14. H.R. Ammar, A.M. Samuel and F.H. Samuel, "Porosity and the fatigue behavior of hypoeutectic and hypereutectic aluminum-silicon casting alloys," *International Journal of Fatigue*, **30**(2008), pp. 1024-1035.
15. L. Liu, A.M.A. Mohamed, A.M. Samuel, F.H. Samuel, H.W. Doty and S. Valtierra, "Precipitation of β -Al₅FeSi Phase platelets in Al-Si based casting alloys," *Metallurgical and Materials Transactions A: Physical Metallurgy and Materials Science*, **40**(2009), pp. 2457-2469.
16. Z. Ma, A.M. Samuel, F.H. Samuel, H.W. Doty and S. Valtierra, "A study of tensile properties in Al-Si-Cu and Al-Si-Mg alloys: Effect of β -iron intermetallics and porosity," *Materials Science and Engineering A*, **490**(2008), pp. 36-51.
17. Z. Ma, E. Samuel, A.M.A. Mohamed, A.M. Samuel, F.H. Samuel and H.W. Doty, "Parameters controlling the microstructure of Al-11Si-2.5Cu-Mg alloys," *Materials and Design*, **31**(2010), pp. 902-912.
18. N. Roy, *M. Eng. Thesis, UQAC, Chicoutimi, Canada* (1995).
19. E. Samuel, B. Golbahar, A.M. Samuel, H.W. Doty, S. Valtierra and F.H. Samuel, "Effect of grain refiner on the tensile and impact properties of Al-Si-Mg cast alloys," *Materials and Design*, **56**(2014), pp. 468-479.
20. Y. Han, A.M. Samuel, H.W. Doty, S. Valtierra and F.H. Samuel, "Optimizing the tensile properties of Al-Si-Cu-Mg 319-type alloys: Role of solution heat treatment," *Materials and Design*, **58**(2014), pp. 426-438.
22. Z. Ma, A.M. Samuel, H.W. Doty, S. Valtierra and F.H. Samuel, "Effect of Fe content on the fracture behaviour of Al-Si-Cu cast alloys," *Materials and Design*, **57**(2014), pp. 366-373.
23. A.M. Samuel, H.W. Doty, S. Valtierra and F.H. Samuel, "Effect of grain refining and Sr-modification interactions on the impact toughness of Al-Si-Mg cast alloys," *Materials and Design*, **56**(2014). pp. 264-273.
24. N. Roy, P.R. Louchez and F.H. Samuel, "Statistical analysis of porosity in Al-9 wt. % Si-3 wt. % Cu-X alloy systems," *Journal of Materials Science*, **31**(1996), pp. 4725-4740.
25. G.E.P. Box, W.G. Hunter and J.S. Hunter, *Statistics for Experimenters*, John Wiley and Sons, Inc., New York (1978).

26. L. Davies, *Efficiency in Research, Development and Production: The Statistical Design and Analysis of Chemical Experiments*, The Royal Society of Chemistry, Cambridge, U.K. (1993).

27. G. Casella, "Statistical Design: Principles, Recommendations and Opinions," Special Report, University of Florida, 2008.

APPENDICES

Table 1: Chemical Composition of the 319.2 Alloy (Wt. %)

Element (wt. %)	Si	Cu	Fe	Mn	Mg	Ti	Sr	Zn	Ni
	6.23	3.77	0.46	0.14	0.06	0.073	0.0003	0.08	0.008

Table 2: Variation in Dendrite Arm Spacing as a Function of Distance from the Chill End in an End-Chill Casting

Distance from Chill End (mm)	Average DAS (μm)
5	15
10	28
20	52
40	73
100	95

Table 3: List of End-Chill Castings Prepared in the Present Work

Series	Castings	Series	Castings
H	H1, H2, H3	HT	H1T, H2T, H3T
	H1S1, H2S1, H3S1		H1TS1, H2TS1, H3TS1
HS	H1S2, H2S2, H3S2	HTS	H1TS2, H2TS2, H3TS2
	H1S3, H2S3, H3S3		H1TS3, H2TS3, H3TS3

Table 4: Chemical Composition of Alloys Used in Directional Solidification

Alloy	Si	Cu	Zn	Fe	Mg	Mn	Ti	Sr	Gr	H
Codes	%	%	%	%	%	%	%	%	%	ml/100 g
H1	5.80	3.80	0.072	0.47	0.01	0.079	0.077	<0.001	0	0.10
H1S1	5.67	2.81	0.077	0.42	0.039	0.067	0.065	0.018	0	0.10
H1S2	6.26	2.98	0.097	0.45	0.038	0.074	0.070	0.018	0	0.10
H1S3	5.76	3.23	0.071	0.47	0.013	0.078	0.075	0.032	0	0.10
H1S1T	5.97	3.29	0.078	0.42	0.014	0.077	0.086	0.009	0.02	0.10
H1S2T	5.97	3.37	0.072	0.47	0.013	0.079	0.088	0.015	0.02	0.10
H1S3T	6.43	3.04	0.066	0.44	0.013	0.071	0.082	0.025	0.02	0.10
H1T	5.81	3.19	0.070	0.45	0.032	0.075	0.091	0.002	0.02	0.10
H2	6.25	3.71	0.083	0.46	0.052	0.13	0.13	<0.001	0	0.22
H2S1	6.23	3.77	0.080	0.46	0.060	0.14	0.073	0.01	0	0.19
H2S2	6.23	3.77	0.080	0.46	0.060	0.14	0.073	0.021	0	0.21
H2S3	6.36	3.74	0.085	0.48	0.050	0.13	0.14	0.025	0	0.25
H2S1T	6.23	3.77	0.080	0.46	0.060	0.14	0.17	0.004	0.02	0.23
H2S2T	6.23	3.77	0.080	0.46	0.060	0.14	0.12	0.011	0.02	0.26
H2S3T	6.23	3.96	0.070	0.511	0.049	0.14	0.148	0.024	0.02	0.24
H2T	6.36	3.76	0.084	0.48	0.051	0.13	0.16	0.013	0.02	0.19
H3	6.24	3.74	0.082	0.47	0.048	0.13	0.073	0.0001	0	0.35
H3S1	6.23	3.77	0.080	0.46	0.060	0.14	0.073	0.009	0	0.33

Table 4: Contd.,										
H3S2	6.23	3.77	0.080	0.46	0.060	0.14	0.073	0.017	0	029
H3S3	6.26	3.74	0.082	0.47	0.046	0.13	0.14	0.029	0	0.35
H3S1T	6.23	3.77	0.080	0.46	0.060	0.14	0.16	0.007	0.02	0.35
H3S2T	6.23	3.77	0.080	0.46	0.060	0.14	0.12	0.009	0.02	0.35
H3S3T	6.22	3.73	0.082	0.047	0.049	0.13	0.19	0.027	0.02	0.34
H3T	6.22	3.73	0.082	0.47	0.050	0.13	0.16	0.0005	0.02	0.30

Table 5: Variation in Percentage Elongation (El.%) as a Function of Alloy Composition, Distance from the Chill End (Mm), and Percent Porosity

Alloy	Distance			Alloy	Distance		
	from chill	El.%	Porosity		from chill	El.%	Porosity
			(%)				(%)
	5	4.5 \pm 0.5	0.014		5	0.85	0.513
H1	20	1.7 \pm 0.16	0.024	H3	20	0.5	1.613
	40	1.1 \pm 0.3	0.212		40	0.4	1.795
	100	0.41	0.505		100	0.13	2.495
	5	4.5 \pm 0.9	0.029		5	1.13	0.582
H1T	20	2.5 \pm 1.0	0.115	H3T	20	0.55	1.974
	40	1.1 \pm 0.8	0.187		40	0.42	2.217
	100	0.85 \pm 0.5	0.363		100	0.27	2.694
	5	3.8 \pm 0.6	0.027		5	1.25	0.892
H1S3	20	2.5	0.150	H3S3	20	0.47	2.638
	40	1.5 \pm 0.5	0.696		40	0.34	2.784
	100	1.0 \pm 0.25	1.183		100	0.28	4.830
	5	3.7 \pm 0.8	0.031		5	0.72	1.187
H1TS3	20	1.8 \pm 0.3	0.214	H3TS3	20	0.55	2.970
	40	1.1 \pm 0.1	0.347		40	0.4	3.226
	100	0.63 \pm 0.2	0.715		100	0.26	3.642

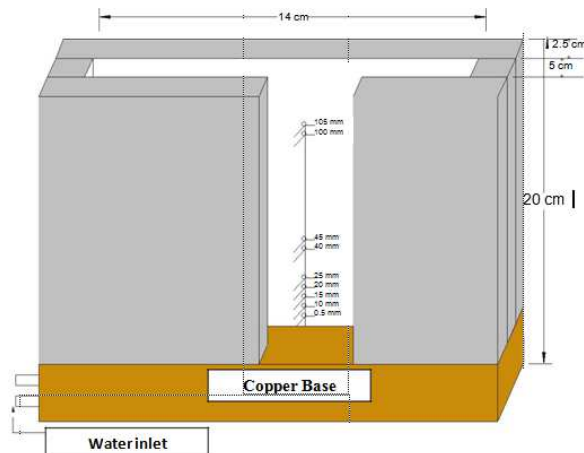


Figure1: Directional Solidification Mold

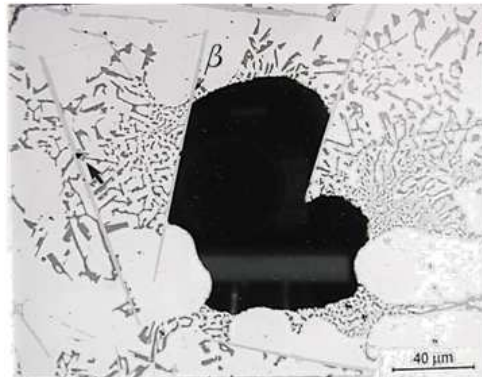


Figure 2: Role of β -Al5FeSi Platelets in Restricting the Growth of a Gas Pore Note the Presence of Small Pores along the Long Sides of the β -Platelets (Arrowed)

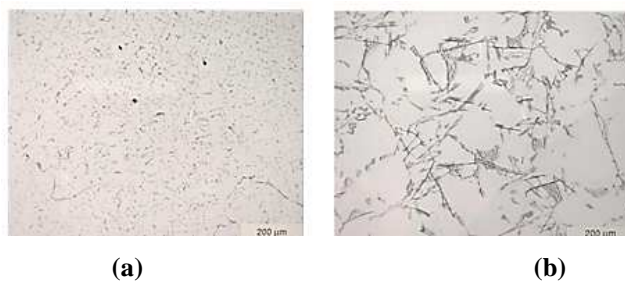


Figure 3: Microstructures of H1 Alloy Samples Obtained at: (A) 5 Mm, (B) 100 Mm Levels above the Chill End Showing the Relative Abundance of β -Al5FeSi Platelets in the Latter Case



Figure 4: Microstructure of H1T Alloy at 100 Mm Distance above the Chill, Showing (A) Thickening of the β -Al5FeSi Needle via a Step-Like Motion of Ledges (Arrowed)

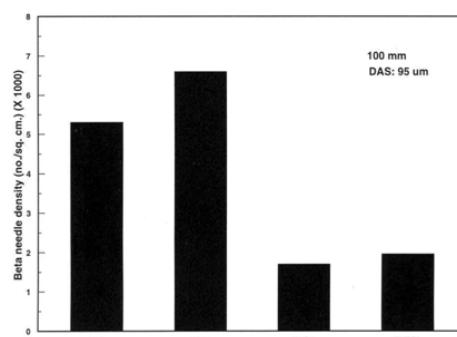


Figure 5: Histogram Comparing the β -Platelets Densities of H1 Alloys at 100 Mm Distance from the Chill End

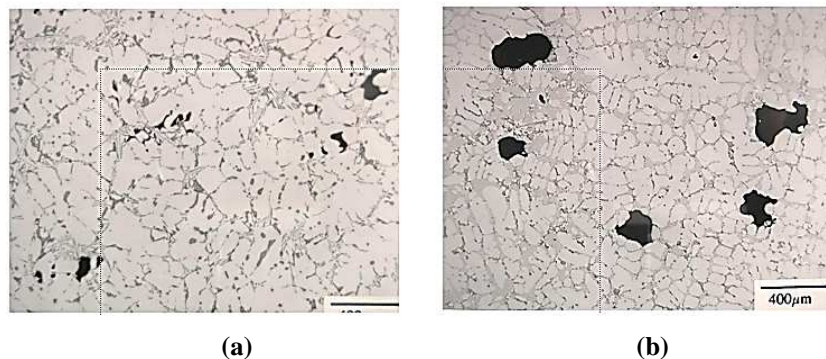


Figure 6: Microstructures Showing Porosity Distribution in: (a) H1 Alloy at 5 Mm, (b) H1 Alloy at 100 Mm, (c) H1S3 Alloy at 100 Mm Distance above the Chill

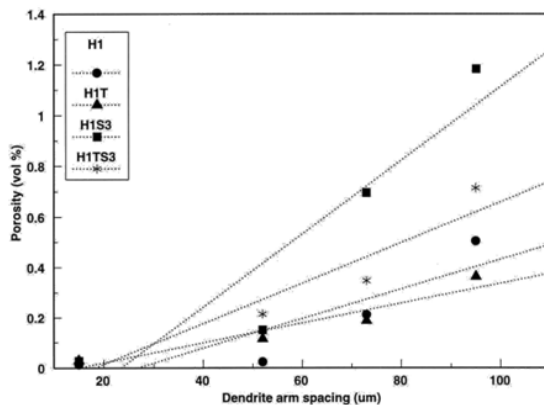


Figure 7: Variation in Percentage Porosity with DAS for H1 Alloys

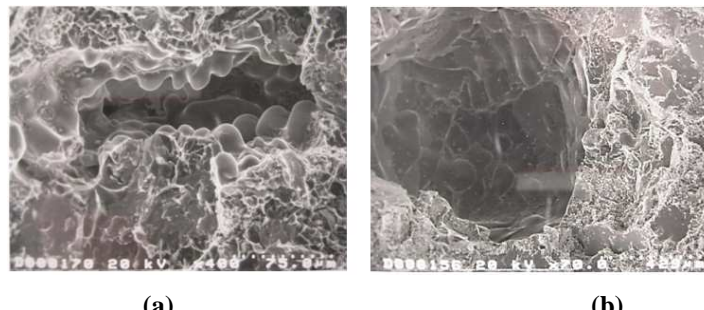


Figure 8: Mic (a) H3 alloy at 5 mm, (b) H3 alloy at 100 mm,

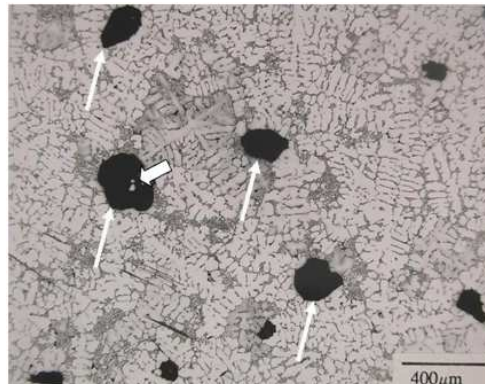
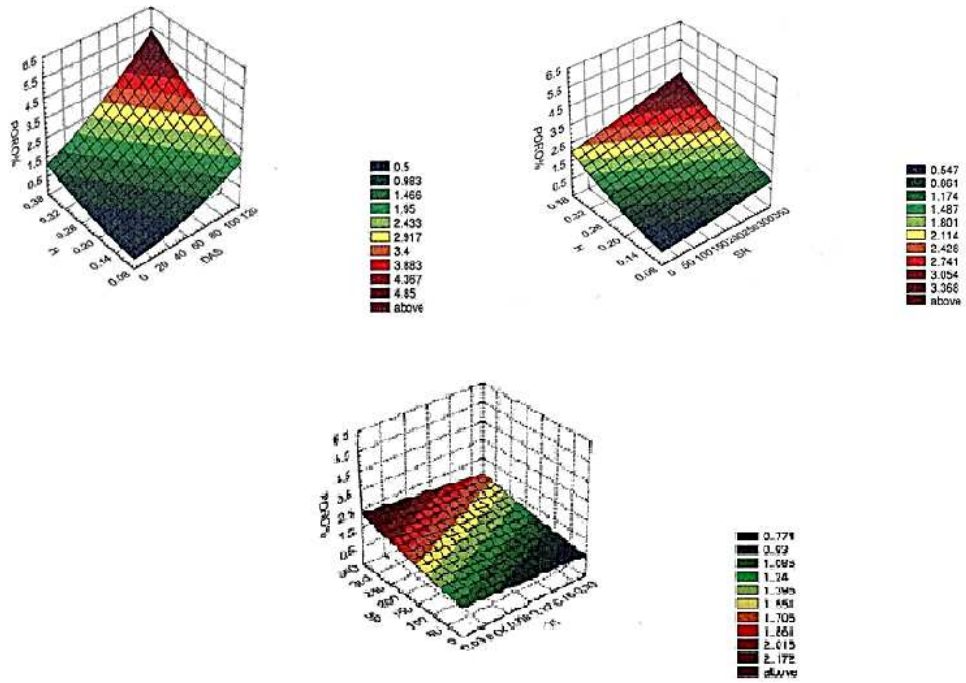


Figure 9: Microstructure Obtained from H3TS3 Alloy and Etched in Keller's Reagent Note the Presence of Porosity at the Grain Boundaries-Arrowed



**Figure 10: the 3D Surface Plots Obtained from Directional Solidification
Showing the Effect of: (a) Cooling Rate, (b) SrAddition, and (c) TiAddition**